Constant Current Charging and Maximum Efficiency Tracking Control Scheme for Supercapacitor Wireless Charging

Zhenjie Li, *Student Member, IEEE*, Kai Song, *Member, IEEE*, Jinhai Jiang, and Chunbo Zhu, *Member, IEEE*

***Abstract*—Charging current and efficiency of a wireless power transfer system depend on the equivalent load resistance of supercapacitor load, which varies during charging. To achieve constant current (CC) charging and maximized efficiency under variable loads, control method that employs primary-side phase shift H-bridge inverter and secondary-side semiactive rectifier are proposed. The proposed secondary-side control method not only achieves CC charging, but also ensures no reactive impedance seen into the semiactive rectifier. Furthermore, the maximum efficiency tracking is based on searching the minimum system dc input current for any given output power. It is realized by phase shift H-bridge inverter that is controlled by the perturbation and observation algorithm. Simulation and experimental results validate the feasibility of the proposed control method. During CC charging of 3 A, the maximum efficiency is 81% and largest efficiency improvement is 15.2% at light load. The proposed control method improves the system performance and is suitable for the applications that require compact receiver and no wireless communication link between the transmitter and the receiver.**

***Index Terms*—Constant current (CC) charging, maximum efficiency tracking, semiactive rectifier, supercapacitor (SC), wireless power transfer (WPT).**

I. Introduction

WIRELESS power transfer (WPT) system for consumer electronic devices and electric vehicles (EV) is gaining more and more attention [1]–[3]. It has the advantages of cordless and automatic charging. In practical, constant current (CC) charging are required by the battery or supercapacitor (SC) load [4]. However, the variation of either equivalent load resistance or mutual inductance affects the charging current and efficiency [5]. Therefore, the motivation of this paper is to analysis and design a WPT system that achieves CC charging and maximum efficiency tracking for SC.

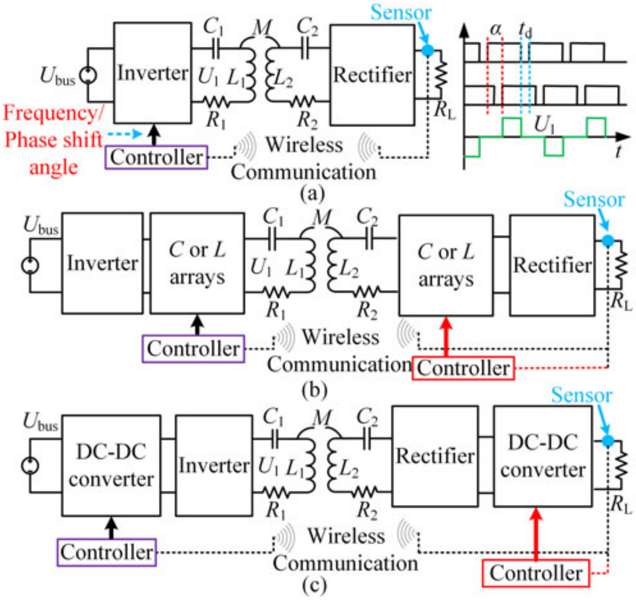

Fig. 1. Circuit diagrams of different control methods for charging current regulation. (a) Variable frequency/phase shift H-bridge inverter, (b) Impedance matching and (c) Dc-dc conversion.

On one hand, CC charging can be realized by properly designing the magnetic coupler and compensation topology. On the other hand, closed-loop control method is essential to maintain the accurate and stable CC charging. As shown in Fig. 1, the widely used methods for charging current regulation are categorized into three groups: variable frequency/phase shift of H-bridge inverter, impedance matching and dc-dc conversion [6]–[10].

Among the control methods shown in Fig. 1, variable frequency control may result in the decrease of power transfer capability and system instability when the operating frequency deviates too much from the peak frequency [6]. Furthermore, the available operating frequency range is regulated by standards and guidelines. The operating frequency for light-duty electric vehicle's wireless charging is 81.38∼90.00 kHz, which is regulated by the society of automotive engineers Task Force's J2954 standard. The operating frequency for portable devices is 110∼205 kHz, which is regulated by Qi standard of wireless power consortium [7], [8]. Impedance matching is commonly

---

Manuscript received July 23, 2017; revised October 11, 2017 and December 5, 2017; accepted January 8, 2018. Date of publication January 15, 2018; date of current version July 15, 2018. This work was supported in part by the National Natural Science Foundation of China under Project Grants 51677032 and 51577034, in part by the Natural Science Foundation of Heilongjiang Province under Grant E2017045, in part by the Harbin Science and Technology Innovation Talents Special Fund Project under Grant 2016RAQXJ002, and in part by the China Postdoctoral Science Foundation under Grant 2014M560254/2015T80338. Recommended for publication by Associate Editor Sanjib Kumar. *(Corresponding author: Kai Song.)*

The authors are with the School of Electrical Engineering and Automation, Harbin Institute of Technology, Harbin 150001, China (e-mail: lizhenjie0725@163.com; kaisong@hit.edu.cn; 306658940@qq.com; zhuchunbo@hit.edu.cn).

Color versions of one or more of the figures in this paper are available online at http://ieeexplore.ieee.org.

Digital Object Identifier 10.1109/TPEL.2018.2793312

applied in high frequency and low power conditions. Due to the bulky and complicated capacitors/inductors matrix, the system size and control complexity increase significantly with power capacity [9]. The primary-side phase shift H-bridge inverter and dc-dc converter require feedback signals from the secondary-side, which may cause instability and control failure if wireless communication link is disturbed by the magnetic field. The secondary-side dc-dc converter avoids the need of wireless communication link. Inevitably, the volume and cost of the receiver are increased, which may be undesirable for some special applications [10]. To solve those drawbacks, secondary-side semiactive rectifier is proposed to adjust the charging voltage [11]. In this paper, the semiactive rectifier is further analyzed, and the improved control method that is compared to [11] is highlighted.

Before designing the WPT system, power inverter and dc-dc converter should be optimized to reduce power losses [12]. Once the WPT system is constructed, impedance matching, magnetic coupler optimization, and load transformation can be applied to further improve the efficiency.

1) *Impedance matching (IM):* Capacitor/inductor matrix or their combination can be used to achieve optimal efficiency when the load resistance and mutual inductance vary. In [13], through switching an adaptive capacitors matrix, maximum efficiency is achieved by using window prediction search algorithm. In [14], automated IM based on the L-match networks is used to increase efficiency through matching the resonant frequency of the magnetic coupler to that of the power source. In [15], an inexpensive auto-adaptive IM rectifier is proposed to improve the efficiency. Those methods are used for high frequency and low power applications. The capacitors/inductors matrix and control circuits increase the volume and control complexity to the WPT system with the increment of power capacity. In addition, the resolution of IM is limited by the discrete capacitor/inductor values.
2) *Magnetic coupler optimization:* With the optimized magnetic couplers such as three or four-coil system and LCC resonant structure, the efficiency can be improved. In [16], the optimization of dual-layer intermediate and implantable coils is proposed to improve the efficiency of a four-coil WPT system. In [17], autotuning algorithm based on a four-coil system is used to track the maximum efficiency against the variation of mutual inductance. In [18], an optimized LCC resonant structure is analyzed to realize a high efficiency for a dynamic WPT system. Although the efficiency can be improved by the optimized magnetic coupler, the drawbacks are that the adjustment range and coil position are limited.
3) *Load transformation:* It is the widely used method for achieving maximum efficiency tracking and can be classified into two types. For type I, through adjusting the duty cycle of dc-dc converter, the equivalent load resistance is regulated to the optimal value that corresponds to the maximum efficiency [22], [23]. The drawback is that the receiver is large and expensive. Wireless communication link is also necessary to feedback the current and voltage information to control the efficiency. For type II, minimum dc input power that provides same output power is searched, then maximum efficiency is achieved [19]. Both buck/boost converter and phase shift H-bridge inverter can be used to realize type II method [20], [21]. The advantage is that wireless communication link is avoided.

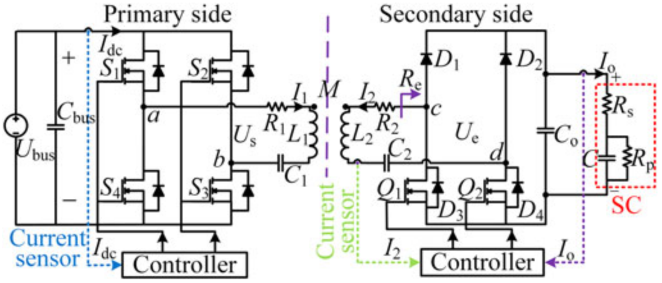

Fig. 2. Structure of the proposed WPT system.

In this paper, control method that has two degree of freedoms, provided by the primary-side phase shift H-bridge inverter and secondary-side semiactive rectifier, is proposed to achieve CC charging and maximum efficiency tracking. As wireless communication link is undesirable, cooperative work between primary-side controller and secondary-side controller is analyzed in depth. This is one of the improvements when compares to previous control methods. At the secondary-side, CC charging is realized by adjusting the PI-controlled semiactive rectifier. For a given output power, maximum efficiency corresponds to minimum system dc input power, which is achieved by adjusting the phase shift H-bridge inverter with perturbation and observation (P&O) algorithm. The rest of the sections are organized as follows: Section II analyzes the system structure and theoretical analysis. Section III presents the operating principle and control strategy of the semiactive rectifier and phase shift H-bridge inverter. Section IV analyzes and verifies the closed-loop control method with simulations. Section V validates the control method with experiments. Finally, the conclusion is summarized in the last section.

II. SYSTEM STRUCTURE AND THEORETICAL ANALYSIS

A. *System Structure*

A WPT system, which consists of the dc voltage source, phase shift H-bridge inverter, magnetic coupler, series-series (SS) compensation, semiactive rectifier, capacitive filter, SC load, and controllers, is separated into two isolated parts namely the primary-side and the secondary-side. As mentioned in [24], among the four basic compensation topologies, only primary-side reactance of SS compensation is independent of both the coupling coefficient variation and load variation when the WPT system operates in resonance. Also, SS compensation is widely used for battery/ SC charging in WPT systems [10], [20].

As shown in Fig. 2, $S_1 \sim S_4$ are four power metallic oxide semiconductor field effect transistors (MOSFET) that constitute the H-bridge inverter. U_{bus} and U_s are the dc input voltage and equivalent ac output voltage of the H-bridge inverter, respectively. L_i, R_i, C_i and I_i $(i = 1, 2)$ are the self-inductance,

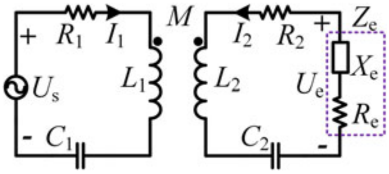

Fig. 3. Mutual inductance model.

internal resistance, compensation capacitance, and resonant current of the primary-side and secondary-side coil, respectively. M is the mutual inductance. The semiactive rectifier consists of two MOSFETs Q_1 and Q_2 with antiparallel diodes D_3 and D_4 in the lower part, and two diodes D_1 and D_2 in the upper part. R_e and U_e are the equivalent input resistance and input voltage seen into the semiactive rectifier, respectively. The circuit model of SC includes a series resistor, R_s, ideal capacitor, C, and parallel resistor, R_p. The system dc input current and output current are measured by Hall current sensors.

B. Optimal Load Condition for Achieving the Maximum Efficiency

The mutual inductance model shown in Fig. 3 is used to perform further analysis.

According to the Kirchhoff's Voltage Law, the WPT system is described as

$$\begin{cases} \left(R_1 + j\omega L_1 + \frac{1}{j\omega C_1}\right) \cdot \dot{I}_1 + j\omega M \cdot \dot{I}_2 = \dot{U}_{\mathrm{s}} \\ j\omega M \cdot \dot{I}_1 + \left(R_2 + j\omega L_2 + \frac{1}{j\omega C_2} + j\mathrm{X}_e\right) \cdot \dot{I}_2 = \dot{U}_e \end{cases} \tag{1}$$

where $\dot{U}_s$, $\dot{U}_e$, $\dot{I}_1$ and $\dot{I}_2$ are the phasors of output voltage of the H-bridge inverter, terminal voltage of $Z_e = R_e + \mathrm{j}X_e$, primary-side and secondary-side current, respectively. ω is the system operating angular frequency and j is the imaginary unit. The losses of H-bridge inverter and active rectifier are ignored to simplify the analysis. Then, the efficiency η, which is defined as the ratio of output power P_{out} to input power P_{in}, is given by

$$\begin{aligned} \eta &= \frac{\mathrm{Re}\left[\dot{U}_e\left(\dot{I}_2\right)^*\right]}{\mathrm{Re}\left[\dot{U}_s\left(\dot{I}_1\right)^*\right]} \\ &= \frac{(\omega M)^2 R_e}{(\omega M)^2 (R_2 + R_e) + R_1\left[(R_2 + R_e)^2 + (X_2 + X_e)^2\right]} \end{aligned} \tag{2}$$

where $X_2 = \omega L_2 - 1/\omega C_2$ is the combined reactance of the secondary-side inductor and capacitor. From (2), it is shown that η is a function of X_2, R_e, and X_e. The larger the $(X_2 + X_e)$ is, the smaller the efficiency η becomes. When the WPT system operates at resonant state, X_2 equals to zero. Then, X_e should be eliminated to achieve the high η. The MATLAB simulations with the parameters listed in Table IV verify the influence of X_e on η. The simulations results are plotted in Fig. 4.

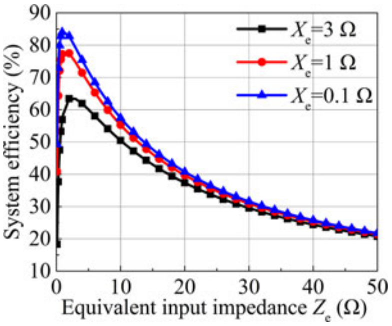

Fig. 4. System efficiency versus different equivalent input impedance Z_e.

As expected, the input voltage and input current are in phase for the full-bridge rectifier, then $Z_e = R_e$ is resistive with $X_e = 0$ [4]. However, for the semiactive rectifier proposed in [11], Z_e is not resistive due to the control strategy. η will be affected by the reactance of Z_e as indicated in Fig. 4. In this paper, the proposed secondary-side control method for the semiactive rectifier ensures CC charging while Z_e is purely resistive. The detailed analysis is explained in Section III-B.

The resonant current is approximately a sine wave due to the high quality factor of resonant tanks [5]. Fundamental harmonic analysis (FHA) has sufficient accuracy for steady-state analysis. The Root Mean Square (RMS) value of U_s that is adjusted by the phase shift H-bridge inverter is deduced as

$$U_s = \left|\dot{U}_s\right| = \frac{2\sqrt{2}}{\pi} U_{\mathrm{bus}} \cos\frac{\alpha}{2} \tag{3}$$

where α is the phase shift angle, as shown in Fig. 1(a). From (3), it is obvious that the relationship between U_s and α is nonlinear. Assuming that the WPT system operates at resonant state and Z_e is resistive to achieve high η, the RMS values of primary-side current and secondary-side current are given by

$$\begin{cases} I_{1\_\mathrm{RMS}} = \frac{(R_2+R_e)}{R_1(R_2+R_e)+(\omega M)^2} \frac{2\sqrt{2}}{\pi} U_{\mathrm{bus}} \cos\frac{\alpha}{2} \\ I_{2\_\mathrm{RMS}} = \frac{(\omega M)}{R_1(R_2+R_e)+(\omega M)^2} \frac{2\sqrt{2}}{\pi} U_{\mathrm{bus}} \cos\frac{\alpha}{2} \end{cases}. \tag{4}$$

Further, the simplified η and R_{e_opt} that corresponds to maximum efficiency $\eta_{\max}$ are expressed as

$$\eta = \frac{(\omega M)^2 R_e}{(R_2 + R_e)^2 R_1 + (\omega M)^2 (R_2 + R_e)} \tag{5}$$

$$R_{e\_\mathrm{opt}} = R_2\sqrt{1 + \frac{(\omega M)^2}{R_1 R_2}} \approx (\omega M)\sqrt{\frac{R_2}{R_1}} \quad \text{for} \quad \eta_{\max}. \tag{6}$$

Based on (5) and the parameters listed in Table IV, η is verified by simulations with different R_e and M, the results are plotted in Fig. 5. It is clear that for either small or large R_e that deviates from R_{e_opt}, η decreases rapidly and $\eta_{\max}$ exists for a fixed M. The larger the M is, the larger the $\eta_{\max}$ is. In practice, actual system efficiency can be calculated by multiplying the efficiency of H-bridge inverter and semiactive rectifier by (5).

C. Secondary-Side Full-Bridge Rectifier and SC Model

For practical applications, the secondary-side rectifier and filter are essential to convert the ac voltage to dc voltage before suppling to the load. As shown in Fig. 2, secondary-side

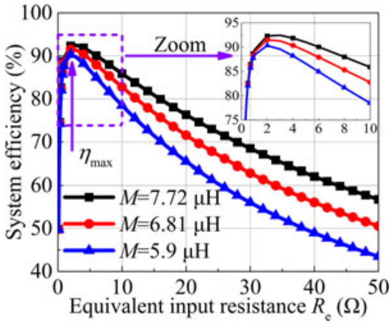

Fig. 5. System efficiency versus different equivalent input resistance R_o and mutual inductance M.

TABLE I
PARAMETERS OF THE SUPERCAPACITOR

Symbol	Quantity	Value
C	Rated capacitance	10 F
R_s	Equivalent series resistance	0.5 Ω
R_p	Equivalent parallel resistance	10 000 Ω
$U_{o\text{-max}}$	Maximum terminal voltage	40 V
U_{o_0}	Initial terminal voltage	10 V

full-bridge rectifier with capacitive output filter is used. The input current and input voltage of the rectifier are sine wave and square wave, respectively. Based on the power balance equation, the relationship between R_e and R_o is given by

$$R_e = \frac{8}{\pi^2} R_o = \gamma R_o. \tag{7}$$

From (7), it is shown that the full-bridge rectifier can realize load transformation while the ratio $\gamma = 0.81$ is a fixed value [19]. Then, the semiactive rectifier is proposed to achieve a variable load transformation ratio. To simplify the analysis, the SC is modeled as a variable resistor that is given by

$$R_o = \frac{U_o(t_1)}{I_o} = \left(R_s + \frac{U_{o\_0}}{I_o}\right) + \frac{T}{C} \tag{8}$$

where $U_o(t_1)$ represents the terminal voltage at time t_1 and U_{o_0} is the initial terminal voltage. From (8), when the charging current I_o is constant, R_o has a linear relationship with the time span T [13]. The SC parameters used in this paper are listed in Table I. Based on (8) and Table I, the value range of R_o is from 4 Ω to 14 Ω within the time span of 100 s. Therefore, it is evident that the WPT system for SC charge is a variable load system.

III. CIRCUIT ANALYSIS FOR THE PROPOSED WPT SYSTEM

This section presents a detailed analysis of the system circuits. First, the load transformation method realized by the secondary-side dc-dc converter is analyzed and the drawbacks are summarized. Second, the semiactive rectifier combined with the optimized control method is proposed to solve the drawbacks of using the dc-dc converter for load transformation. Compared with the method analyzed in [11], the improvement of the proposed secondary-side control method is highlighted. Finally, the cooperative work between the phase shift H-bridge inverter and semiactive rectifier is illustrated to verify the feasibility of the proposed control method.

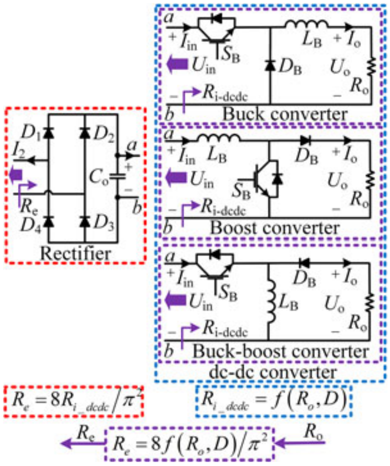

Fig. 6. Different dc-dc converters for load transformation.

TABLE II
DC-DC CONVERTERS FOR LOAD RESISTANCE ADJUSTMENT

Converter type	Voltage ratio $U_{\text{out}}/U_{\text{in}}$	Load resistance transformation R_e/R_o
Buck	D	$8/(\pi D)^2$
Boost	$1/(1-D)$	$8(1-D)^2/\pi^2$
Buck-boost	$-D/(1-D)$	$8(1-D)^2/(\pi D)^2$
SEPIC	$D/(1-D)$	$8(1-D)^2/(\pi D)^2$

A. Analysis of Using DC-DC Converters for Load Transformation

As analyzed in Section II-C, R_o varies over time, which influences η. As shown in Fig. 6, different dc-dc converters such as buck, boost, and buck-boost converter can be used to realize the load transformation. R_e is regulated by the duty cycle D of the dc-dc converter [19]. Take buck converter for example, the relationship between the input voltage U_{in} and the output voltage U_o is expressed as

$$U_o = DU_{\text{in}}. \tag{9}$$

The power losses of buck converter are ignored to simplify the analysis. Based on the power balance equation and (9), R_e seen into the full-bridge rectifier is given by

$$R_e = \frac{8}{\pi^2} R_{i\_\text{buck}} = \frac{8}{\pi^2 D^2} R_o. \tag{10}$$

Through adjusting D, R_e is regulated to R_{e_opt}, and then $\eta_{\max}$ is tracked. The above analysis is also suitable for other dc-dc converters that are listed in Table II.

Due to limited range of D, different dc-dc converters have different load transformation range. Combined with the system parameters listed in Table IV, $\eta_{\max}$ tracking that is realized by different dc-dc converters are verified and the simulation

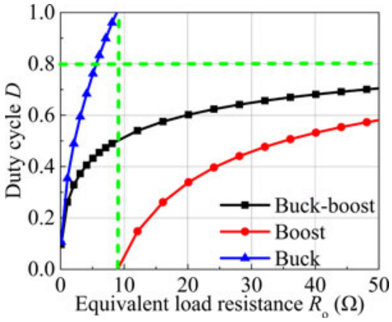

Fig. 7. Load transformation range of different dc-dc converters.

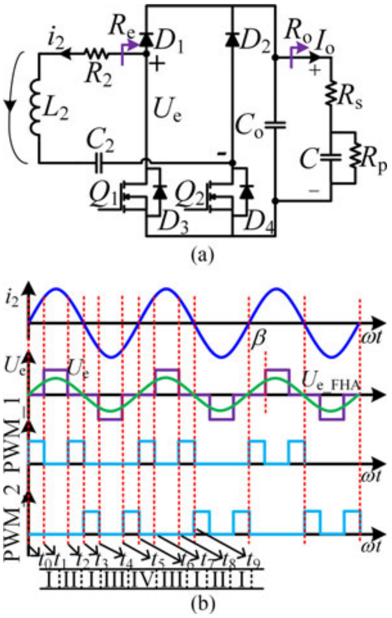

Fig. 8. Proposed secondary-side semi-active rectifier. (a) Circuit diagram and (b) operating waveforms.

results are plotted in Fig. 7. It is shown that buck and boost converters realize $\eta_{\max}$ tracking within 0∼8.7 Ω and 8.7 Ω∼+∞, respectively. Buck-boost converter achieves $\eta_{\max}$ within the full load range of 0∼+∞. Therefore, buck-boost converter is preferred for used due to its wide adjustable load range.

For practical applications, the selection of dc-dc converters depends on the range of R_o that depends on the load and the available D which is limited by the accuracy of the controller and MOSFET/IGBT driver. Furthermore, the dc-dc converter imposes additional volume, cost and power losses on the receiver. Therefore, an alternative method of the semiactive rectifier is proposed to avoid the drawbacks of the dc-dc converter, which is analyzed as follows.

B. Operating Principle of the Secondary-Side Semiactive Rectifier

As shown in Fig. 8(a), when compares to the dc-dc converter, the semiactive rectifier reduces an inductor and a filter capacitor that occupy large space and add to the weight of the receiver. To simplify the analysis, the diodes and MOSFETs are assumed to be ideal. The capacitive filter C_o is also assumed to be lossless and is large enough to maintain the constant dc voltage. The operating waveforms are plotted in Fig. 8(b) and operating modes are listed in Table III. (Note: i_2 is the secondary-side resonant current, U_e is the input voltage seen into the semiactive rectifier, U_{e_FHA} is the fundamental component of U_e, PWM_1 and PWM_2 are the driving signals for MOSFET Q_1 and Q_2).

TABLE III
OPERATING MODES OF THE PROPOSED SEMI-ACTIVE RECTIFIER

Operating modes	MOSFETS	Diodes	The power transferred to the supercapacitor
I	Q_1 on, D_4 on	D_1 off, D_2 off	No, circulating in the resonant tank
II	D_1 on, D_4 on	Q_1 off, Q_2 off	Yes, transferred to supercapacitor
III	Q_2 on, D_3 on	D_1 off, D_2 off	No, circulating in the resonant tank
IV	D_2 on, D_3 on	Q_1 off, Q_2 off	Yes, transferred to supercapacitor

As analyzed in Section II-B, if the impedance Z_e seen into the semiactive rectifier is not resistive, η will be affected. Through the proposed secondary-side circuit and control method, i_2 can be in phase with both u_e and its fundamental component u_{e_FHA}, as shown in Fig. 8(b). Then, R_e is purely resistive, which ensures high η. This is the improvement when compares to the method analyzed in [11]. Fig. 8(b) also shows that one operating sequences consists of Mode I-II-I-III-IV-III and the driving signals PWM_1 and PWM_2 are obviously different from [11]. The control circuit used for generating the driving signals is further analyzed in Section IV-B.

During one operating period, u_e has three possible stages and is expressed as

$$u_e = \begin{cases} 0, & -\beta < \omega t < \beta \\ U_o, & \beta < \omega t < \pi - \beta \\ 0, & \pi - \beta < \omega t < \pi + \beta \\ -U_o, & \pi + \beta < \omega t < 2\pi - \beta \end{cases} \tag{11}$$

where β is the phase shift angle of the semiactive rectifier and U_o is the SC terminal voltage. Based on FHA, the RMS value of u_e is given by

$$u_{e\_\mathrm{RMS}} = \frac{2\sqrt{2}}{\pi} U_o \cos\frac{\beta}{2}. \tag{12}$$

From (12), it is shown that through adjusting β, u_{e_RMS} and the power transferred to the SC is adjusted. Based on the power balance equation, R_e is deduced as

$$R_e = \frac{u^2_{e\_\mathrm{RMS}}}{u^2_o / R_o} = \frac{8}{\pi^2} R_o \cos^2\frac{\beta}{2}. \tag{13}$$

According to (6), when $\eta_{\max}$ is achieved, (13) is derived as

$$R_o \cos^2\frac{\beta}{2} = \frac{\pi^2 R_2}{8}\sqrt{1 + \frac{(\omega M)^2}{R_1 R_2}} \approx \frac{\pi^2 (\omega M)}{8}\sqrt{\frac{R_2}{R_1}}. \tag{14}$$

Once the WPT system is designed, the items on the right side of (14) are fixed, the variation of R_o can be adjusted by β.

TABLE IV
SYSTEM PARAMETERS OF THE EXPERIMENTAL SETUP

Symbol	Quantity	Value
L_1	Primary-side coil inductance	56.9 μH
R_1	Primary-side coil resistance	0.16 Ω
ϕ_1	Primary-side transmitter diameter	10 cm
L_2	Secondary-side coil inductance	36.2 μH
R_2	Secondary -side coil resistance	0.1 Ω
ϕ_2	Secondary-side transmitter diameter	7 cm
d	Rated transfer distance	3 cm
k	Rated coupling coefficient	0.15
M	Rated mutual inductance	6.8 μH
f_s	System operating frequency	85.5 kHz
U_{bus}	System dc input voltage	48 V
I_o	Charging current	3 A

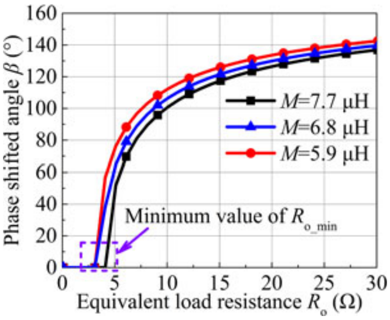

Fig. 9. Semi-active rectifier for the maximum efficiency tracking.

Because $\cos^2(\beta/2)$ is limited to 0∼1, R_o is limited by (15).

$$R_o \geq \frac{\pi^2(\omega M)}{8}\sqrt{\frac{R_2}{R_1}}. \tag{15}$$

According to the system parameters listed in Table IV, simulation results of (15) are plotted in Fig. 9.

As shown in Fig. 9, Only when R_o is larger than a specific value $R_{o\_\min}$, the semiactive rectifier is able to track $\eta_{\max}$. Take $M = 6.8\,\mu$H for example, the semiactive rectifier starts to track $\eta_{\max}$ when $R_{o\_\min} > 3.6\,\Omega$. Then, it is clear that system parameters should be properly designed to ensure the normal system operation for different applications.

C. Cooperative Work of the Phase Shift H-Bridge Inverter and Semiactive Rectifier

In general, the parameters of the WPT systems are in dynamic correlation [25]. For instance, the variation of R_o will influence both I_o and η. The detailed analysis about the cooperative work of CC charging and $\eta_{\max}$ tracking is illustrated as follows. The adjustment of β not only realizes the load transformation for tracking $\eta_{\max}$, but also influences the power transferred to the SC. Therefore, the semiactive rectifier can be used to adjust I_o. On this basis, one more degree of freedoms is required to regulate η. The primary-side phase shift H-bridge inverter is introduced to track $\eta_{\max}$. According to (4) and (5), I_o and η are further expressed as

$$I_o = \frac{8U_{\text{bus}}(\omega M)}{R_1(R_2\pi^2 + 8R_o\cos^2\frac{\beta}{2}) + (\omega M)^2\pi^2}\cos\frac{\alpha}{2}\cos\frac{\beta}{2} \tag{16}$$

$$\eta = \frac{(\omega M)^2 8\pi^2 R_o\cos^2\frac{\beta}{2}}{\left(R_2\pi^2 + 8R_o\cos^2\frac{\beta}{2}\right)^2 R_1 + (\omega M)^2\left(R_2\pi^4 + 8\pi^2 R_o\cos^2\frac{\beta}{2}\right)}. \tag{17}$$

From (16) and (17), I_o is a function of α, β, and R_o, and η is a function of β and R_o. It is evident that I_o is also related to η, which further verifies that the primary-side and secondary-side control methods should be cooperative. When R_o varies during charging, CC charging and $\eta_{\max}$ tracking can be realized by the coordinate regulation of α and β. For a fixed I_{o_set}, when $\eta_{\max}$ is tracked, α is deduced as

$$\alpha = 2\arccos\left(\frac{I_{o\_\text{set}}\left(\pi^2 A + (\omega M)^2\pi^2\right)}{8U_{\text{bus}}(\omega M)\sqrt{\frac{\pi^2 R_2}{8R_o}\sqrt{1+\frac{(\omega M)^2}{R_1 R_2}}}}\right)$$

$$A = R_1R_2 + \sqrt{(R_1R_2)^2 + (R_1R_2)(\omega M)^2}. \tag{18}$$

When no wireless communication link is desired, CC charging is realized by measuring I_o at the secondary-side directly, and $\eta_{\max}$ is tracked by measuring the minimum I_{dc} at the primary-side. In practice, two methods that are divided into model-based approach and P&O algorithm can be used to realize the above goals.

Model-based approach: CC charging is achieved by adjusting β of the PI controlled semiactive rectifier. α for $\eta_{\max}$ tracking is calculated by (18) in the processor. The advantages are that primary-side current/voltage sensors and $\eta_{\max}$ tracking algorithm are not needed. However, the effectiveness of this method depends on the microprocessor performance. Also, the execution of (18) requires substantial computations and time, which may be undesired for high control speed conditions. Furthermore, due to the system parameters drift and inaccurate measurements, this method may not predict $\eta_{\max}$ accurately [5].

P&O algorithm: This method is derived from the concept of maximum power point tracking in photovoltaic generation applications [26]. Similar to model-based approach, CC charging is realized by adjusting β of the PI controlled semiactive rectifier. On the other hand, $\eta_{\max}$ is achieved by measuring the minimum system dc input current I_{dc} when U_{bus} is fixed. This is the main difference when compares to the model-based approach. The advantages are that high-performance processor is not required and the P&O algorithm is proven. Because I_{dc} is measured in real-time, the accuracy of $\eta_{\max}$ is high. Therefore, this method is analyzed in depth.

IV. ANALYSIS OF THE PROPOSED PRIMARY-SIDE CONTROLLER

Fig. 10 shows the control diagram of the proposed WPT system. On the primary side, the current sensor placed at the dc input port of the phase shift H-bridge inverter measures the dc

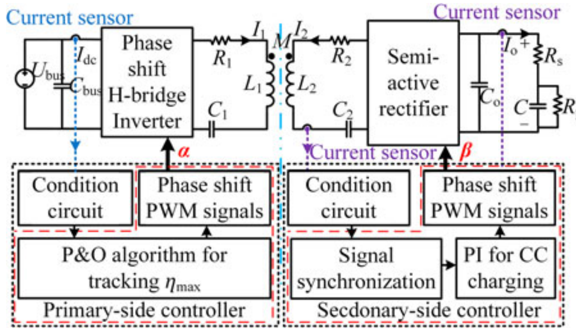

Fig. 10. Control diagram of the proposed WPT system.

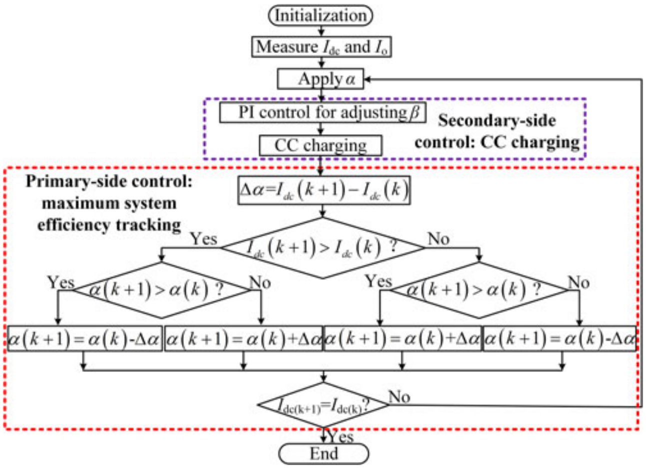

Fig. 11. Flow chart of the proposed control method.

input current I_{dc}. η_{max} is then tracked by the P&O algorithm. In [26], it points out that P&O algorithm is easy to be realized in most of the microcontrollers without extra computational burden. On the secondary side, I_o is measured and feedback to the controller, and CC charging is realized by the PI controlled semiactive rectifier. Here, the PI controller is used for its simple structure and high robustness. Furthermore, the current of secondary-side resonant tank is measured to synchronize the PWM signals for driving the semiactive rectifier, which is explained in Section IV-B.

A. *Operating Principle Analysis*

Through the signal synchronization circuit that is shown in Fig. 10, the operating frequency of the semiactive rectifier is synchronized to the secondary-side resonant frequency and much faster than the variation of R_o. Then, during the iterative searching of $\eta_{\max}$, R_o is assumed to be constant. CC charging is realized by the semiactive rectifier, and then output power is constant for a short time. For fixed U_{bus}, the minimum I_{dc} that corresponds to $\eta_{\max}$ is searched by adjusting α of the phase shift H-bridge inverter [27]. Furthermore, it is reasonable to ensure that the system input power is sufficient for the maximum load power. The flow chart that is shown in Fig. 11 is described as follows:

1) Initial, α_0 is applied and the power is sufficient to charge the SC. CC charging is realized by adjusting β of the PI controlled semiactive rectifier. The initial β is denoted as β_0.
2) During 1), the initial I_{dc0} is measured and recorded in the primary-side controller. The P&O algorithm is used to track $\eta_{\max}$. Through decreasing or increasing α to a new value $\alpha_1 = \alpha_0 - \Delta\alpha_i$ or $\alpha_1 = \alpha_0 + \Delta\alpha_i$, I_{dc} increases or decreases to a new value $I_{dc1} = I_{dc0} + \Delta I_{\text{dc}}$ or $I_{dc1} = I_{dc0} - \Delta I_{\text{dc}}$. The change of I_{dc} induces the variation of the power transferred to SC, and I_o varies accordingly.
3) The new α of H-bridge inverter is denoted as α_1, and then β is adjusted to realize CC charging again. Now the new β is denoted as β_1. Again, the new I_{dc1} is measured and recorded in the primary-side controller.
4) Compares I_{dc1} with I_{dc0}. Smaller I_{dc1} compared to I_{dc0} indicates that η is increased. Keep searching in this direction and repeat steps 2) and 3) until I_{dc} increases. If I_{dc1} is larger than I_{dc0}, meaning that η is decreased, reverse the searching direction and repeat steps 2) and 3) until I_{dc} stop decreasing. $\eta_{\max}$ is successfully tracked by the P&O algorithm.

When $\eta_{\max}$ is tracked, steps 2) to 4) may repeat several times to eliminate the errors that are caused by the signal noises and measurement errors. One of the difficulty in realizing the control method is to make sure that the control of semiactive rectifier and phase shift H-bridge inverter operates steadily to achieve CC charging and track $\eta_{\max}$ simultaneously.

B. *Simulation Analysis*

The circular type magnetic coupler is used in the WPT system. Finite element analysis simulations based optimization are performed prior to fabricate it. The magnetic coupler is designed to reduce the influence of misalignment on η and I_o. M versus vertical and horizontal misalignments are obtained by Ansys Maxwell software and Keysight E4990A Impedance Analyzer. The parameters of the magnetic coupler are plotted in Fig. 12(a). Fig. 12(b) shows that M decreases with the increment of misalignment. With the aid of larger transmitter and smaller receiver, the influence of horizontal misalignment on M is relatively small within specific range. It is also noted that the simulation results are consistent with the experimental results, and the error is less than 3%.

Once the magnetic coupler is optimized, the control circuit will be analyzed. Fig. 13(a) shows that secondary-side control circuit consists of PWM signal generation unit that drives the MOSFETs of the semiactive rectifier and PI controller that achieves CC charging for SC. Through detecting the zero crossing points of i_2, the logic circuits that consist of comparators and NOR gates generate PWM_1 and PWM_2.

As shown in Fig. 13(b), input voltage and input current of the semiactive rectifier are synchronized to the same phase. Then, R_e is resistive seen into the semiactive rectifier. The proposed secondary-side control method can be easily realized by analog circuit and no processor is required, which is suitable for compact and low cost receiver. Compared with the method analyzed

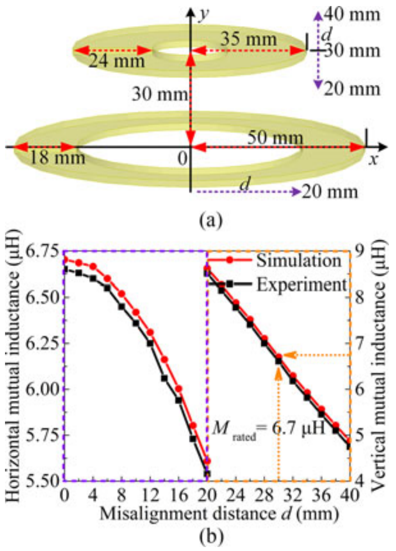

Fig. 12. Misalignment analysis for the magnetic coupler. (a) Simulation model. (b) Simulation and experimental results.

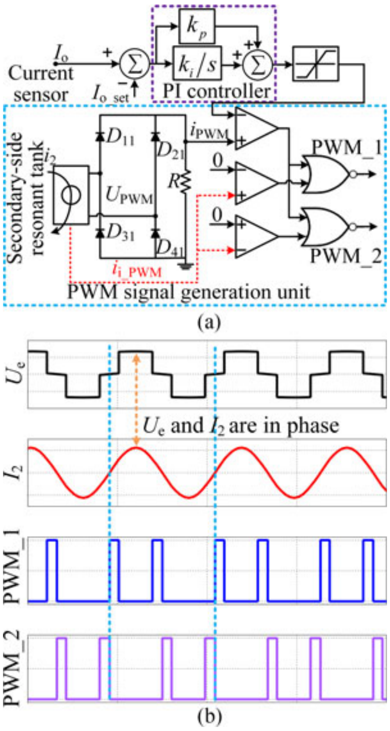

Fig. 13. Control circuit for the semi-active rectifier. (a) Circuit diagram and (b) Simulation waveforms.

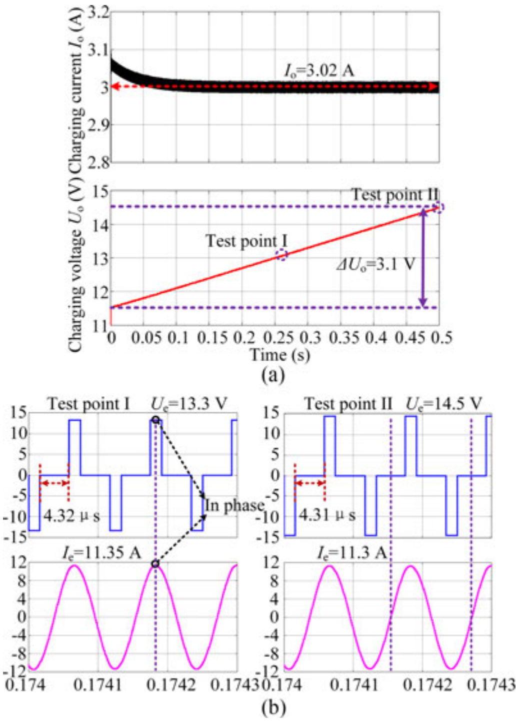

Fig. 14. Simulations of CC charging. (a) Charging current and terminal voltage and (b) Input voltage and input current of the semi-active rectifier.

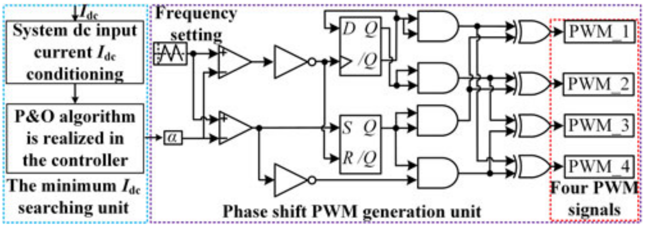

Fig. 15. Primary-side control circuit for the maximum efficiency tracking.

in [11], the proposed secondary-side control method is much more easy and simple. This is one of the improvements for the semi-active rectifier in this paper.

The closed-loop simulations are performed on the computer with Windows 7 Ultimate 64 Bit operating system, 32 G RAM and Intel Xeon(R) CPU E5-2620 0@ 2.00 GHz processor. Considering the performance of central processing unit (CPU) and the resolution of software simulation, substantial time is required to conduct the dynamic Simulink simulations. Then, the feasibility of CC charging is verified with the following parameters: α is 90°, charging time t is 0.5 s, ideal capacitance is 0.5 F and other system parameters are the same with Table IV. As shown in Fig. 14(a), U_o increases linearly with t, which is coincident with the SC charging profile. Fig. 14(b) shows that CC charging is achieved by decreasing β.

Primary-side control circuit for $\eta_{\max}$ tracking is shown in Fig. 15. The P&O algorithm is implemented by the controller, then α is obtained. Further, phase shift PWM generation unit generates four PWM signals for the H-bridge inverter.

When the minimum I_{dc} is tracked by adjusting $\alpha, \eta_{\max}$ is tracked during CC charging. The main difficulty of primary-side control method is to realize the P&O algorithm. In the future works, improved P&O algorithms that are proven and widely used in photovoltaic generation applications could be applied to the proposed WPT system. Then, the system will be more suitable for practical applications.

Further, the feasibility of $\eta_{\max}$ tracking is verified by the simulations that are shown in Fig. 16. Through adjusting α and $\beta, \eta_{\max}$ is 85.7% when U_o is 30 V. Note that a system parameters

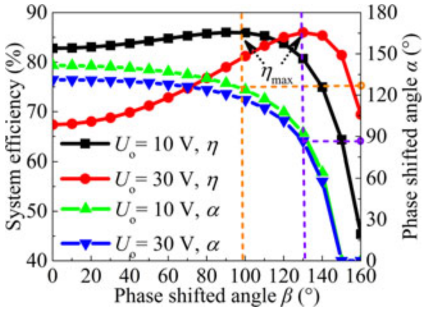

Fig. 16. Simulations curves for the maximum efficiency tracking.

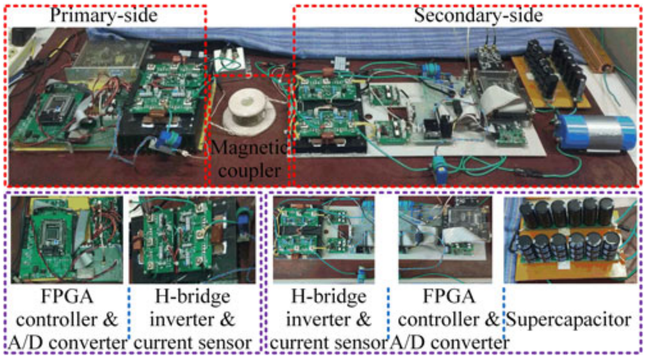

Fig. 17. Experimental setup of the proposed WPT system.

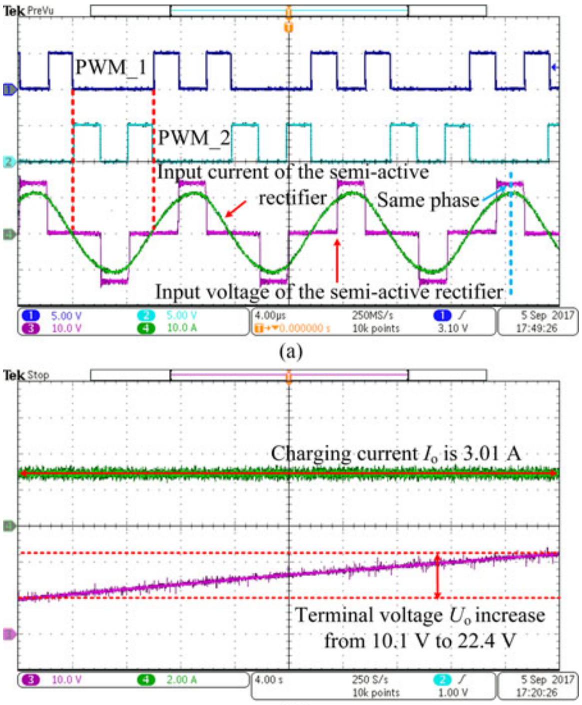

Fig. 18. Secondary-side operating waveforms. (a) Input voltage/current and PWM signals of the semi-active rectifier and (b) Charging current and terminal voltage of the supercapacitor.

need be properly designed to ensure controllability and stability of the WPT system during whole charging process.

V. EXPERIMENTAL EVALUATION

Based on the above analysis, experiments have been carried out to evaluate the performance of the proposed WPT system. Fig. 17 shows the experimental setup in the laboratory. The system parameters are listed in Table IV. Note that the designed experimental setup is used to verify the feasibility of the proposed control method. According to different practical applications, the size and power capacity of the experimental setup should be scale down/up. Also, different controllers can be selected by actual demands such as cost and control speed.

A. Experimental Setup

As shown in Fig. 17, the power flows into the phase shift H-bridge inverter (MOSFETs: Infineon IPW60R041C6 and freewheeling diodes: FAIRCHILD RHRP3060) from the system dc input port. The dc voltage is transformed to ac voltage, then ac voltage is transferred to the secondary-side by the optimized magnetic coupler (Litz wire: diameter of 0.1 mm and 300 strands). The semiactive rectifier (MOSFETs: Infineon IPW60R041C6 and diodes: FAIRCHILD RHRP3060) and capacitive filter (film capacitor) convert the ac voltage to dc voltage, and then supplies to the SC.

The realization of the proposed control method is described as follows. P&O algorithm is realized by the primary-side field programmable gate array (FPGA) controller (Altera Cyclone IV EP4CE6F17C8N). Four PWM signals with phase shift angle α are generated to track $\eta_{\max}$. The primary-side FPGA controller also realizes the system soft start and the detects system operation state. When the over-voltage/current and system failures occur, WPT system shuts down safely. Based on the PWM synchronization circuit, the secondary-side FPGA controller generates two PWM signals with phase shift angle β for the PI controlled semi-active rectifier, then CC charging is realized.

B. Experimental Results of the Proposed Control Method

First, CC charging that is achieved by the secondary-side semiactive rectifier is verified. The experimental waveforms are captured by using Tektronix Oscilloscope MDO3045B. Fig. 18(a) shows that the input voltage and input current of the semiactive rectifier have the same phase, which is consistent with the simulation results shown in Fig. 14(b). Fig. 18(b) shows that within the time span of 40 s, I_o is maintained constant and the increment of U_o is 12.3 V.

During CC charging, the primary-side control method that realizes $\eta_{\max}$ tracking is verified. The experimental results are shown in Fig. 19. The principle is that $\eta_{\max}$ can be tracked by searching the minimum $I_{\rm dc}$. The searching process starts at stage I, $I_{\rm dc}$ decreases through adjusting α that is generated by PWM_1 and PWM_3 signals. The minimum $I_{\rm dc}$ is obtianed at t_1. For stage II, the searching process repeats once to elimate the errors that are caused by a system noises and current sensors. Finally, the minimum $I_{\rm dc}$ is tracked at t_2.

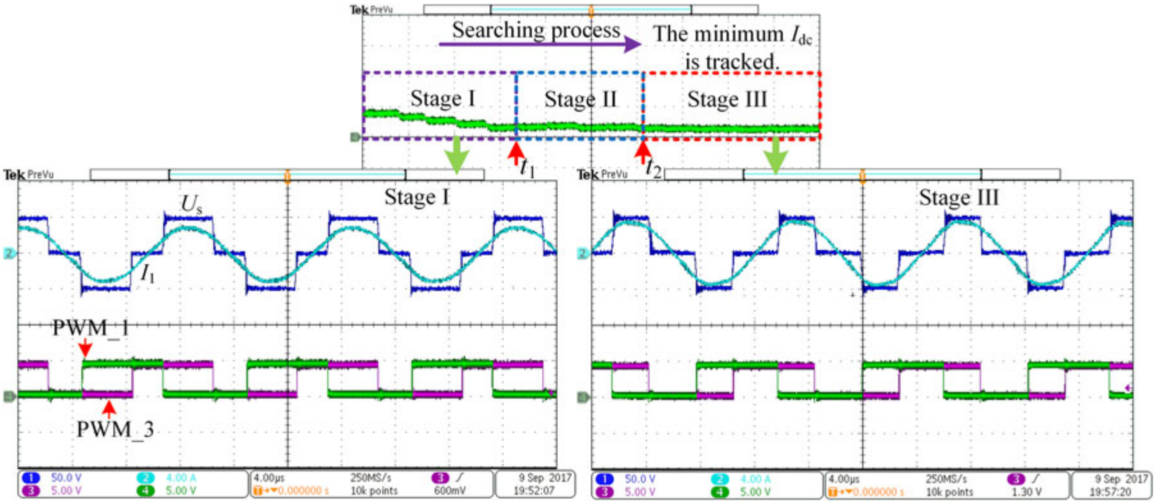

Fig. 19. Experimental waveforms of the maximum efficiency tracking (U_s is the H-bridge inverter's output voltage and I_1 is the primary-side current).

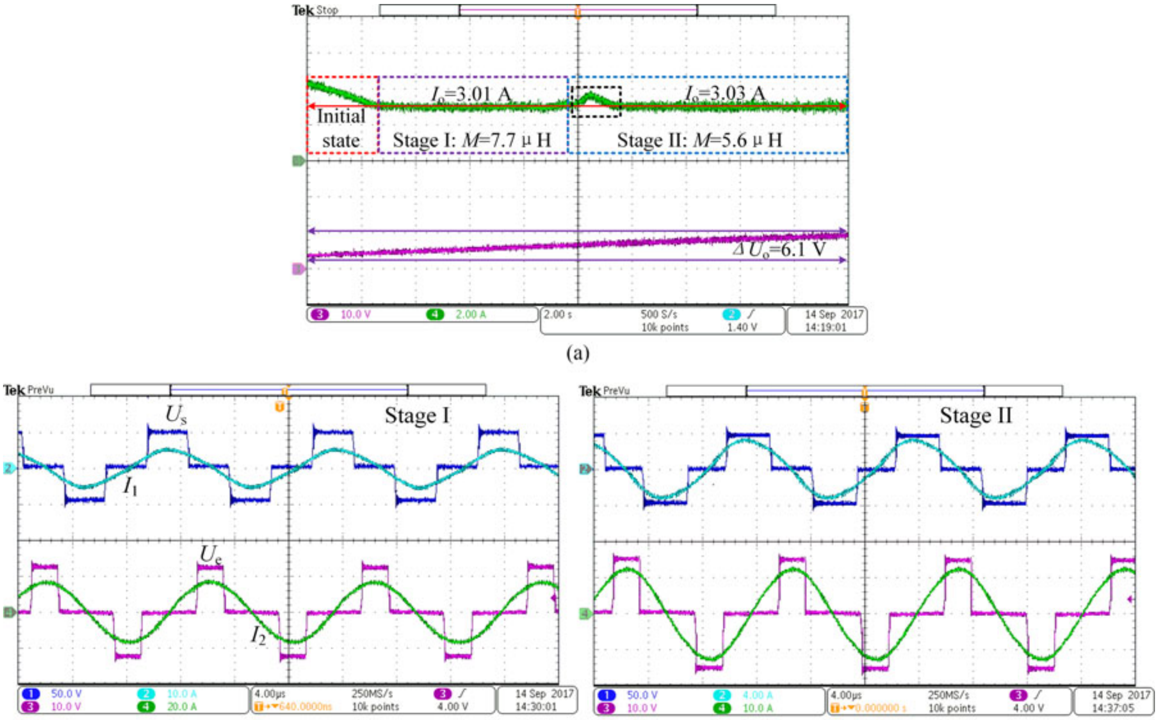

(a)

(b)

Fig. 20. Experimental results when misalignment occurs. (a) Charging current and terminal voltage of the supercapacitor and (b) Output voltage U_s and current I_1 of the phase shift H-bridge inverter, input voltage U_e and current I_2 of the semi-active rectifier.

Combined with Figs. 18 and 19, it is known that the correctness of the proposed control method is verified. Furthermore, the influence of misalignment on the proposed control method is analyzed in Section V-C. Also, the power losses are measured to provide references for the future system optimization works.

C. Influence of Misalignment on the Proposed Control Method

In practice, the misalignment that causes the variation of M is inevitable. Then, the vertical position of the receiver varies from 24 to 36 mm that corresponds to M changes from 7.7 μH to 5.6 μH is verified. The waveforms are shown in Fig. 20.

Fig. 20(a) shows that the proposed control method is still effective even when misalignment occurs. At the initial state, the secondary-side PI controller begins to work, and then I_o decreases to the preset 3 A. At the beginning of stage II, M changes from 7.7 μH to 5.6 μH and a slight fluctuation of I_o occurs. Through the PI controlled semi-active rectifier, I_o is constant. Within the time span of 20 s, the increment of U_o is 6.1 V. Fig. 20(b) shows that the combination of α and β is adjusted to track $\eta_{\max}$. Note that the misalignment should be set within a suitable range, so as to ensure the normal system operation. When the misalignment is too large, the proposed

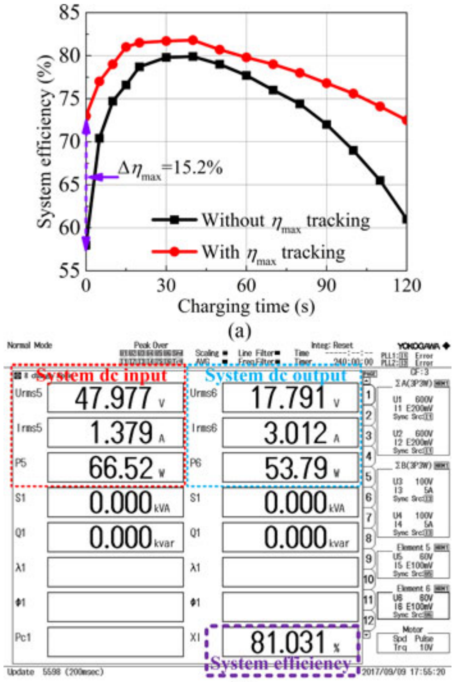

Urms5 47.977 V
Irms5 1.379 A
P5 66.52 W
S1 0.000 kVA
Q1 0.000 kvar
λ1
Φ1
Pc1

Urms6 17.791 V
Irms6 3.012 A
P6 53.79 W
S1 0.000 kVA
Q1 0.000 kvar
λ1
Φ1
X1 81.031 %

Update 5598 (200msec)
2017/09/09 17:55:20

(b)

Fig. 21. Experimental results of the system efficiency $(k = 0.15)$. (a) System efficiency comparison and (b) Print screen when $\eta_{\max}$ is tracked.

control method may not work properly. Therefore, a system parameters (such as the magnetic coupler, the system dc input voltage, and the SC voltage) should be welly optimized to ensure the stability and reliability of the WPT system.

D. System Efficiency and Losses Analysis

During the charging process, system efficiency from the system dc input to the SC is measured by the Yokogawa WT1800 power analyzer. Channel 5 and channel 6 measures the system dc input power and power of the SC, respectively. The measured curves and print screen are shown in Fig. 21. Fig. 21(a) shows that the system efficiency can be significantly improved by the proposed $\eta_{\max}$ tracking method and the largest improvement $\Delta\eta_{\max}$ is 15.2% at light load. When $\eta_{\max}$ is tracked, the print screen of Yokogawa WT1800 power analyzer is shown in Fig. 21(b). The measured $\eta_{\max}$ and I_o are 81% and 3.01 A, respectively. In addition, it is pointed out that the accuracy of experimental results are limited by the accuracies of the controller and current sensors.

The system losses that consist of H-bridge inverter losses (turn on/ off losses and conduction losses), magnetic coupler losses (coil losses and core losses), semiactive rectifier losses (turn on/off losses and conduction losses), and other losses are measured [28]. The experimental results are shown in Fig. 22. It is obvious that the losses of H-bridge inverter and magnetic coupler constitute the bulk of the system losses. Therefore, the design of H-bridge inverter and magnetic coupler is vital to improve the system performance. In practice, the winding materials and switching components with low resistivity can be adopted to reduce the losses, such as the silicon carbide MOSFET can be selected for its favorable switching losses characteristic [29].

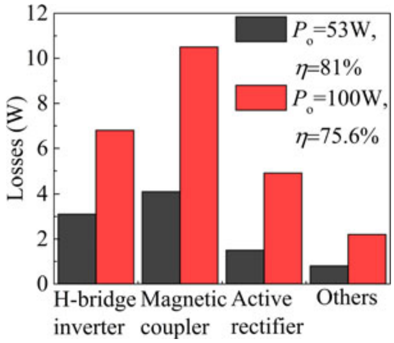

Fig. 22. System Losses analysis under different power conditions.

E. Comparison to Previous Control Methods

In recent years, different control methods for achieving constant current/voltage charging and $\eta_{\max}$ tracking are reported. The parameters and results of their experimental prototypes are summarized and listed in Table V. Due to the different system parameters and circuit structures are used for each setup, a fair comparison among those control methods is difficult to obtain. Then, the emphasis of this paper is focused on the simplification of secondary-side circuit and the design of no wireless communication link. Compared with dc-dc converter, the semi-active rectifier avoids an inductor and a filter capacitor that are heavy and space occupying at secondary side. Furthermore, the proposed control method avoids the wireless communication link that is required by most of the control methods listed in Table V. Without wireless communication link, the system can be more stable.

In practice, the proposed control method is suitable for both low power applications such as portable devices and high power applications such as EVs. Take Qi product for example, the rectification circuit of the receiver can be full-bridge rectifier that consists of four diodes and synchronous rectifier that consists of four MOSFETs [30], [31]. Although the usage of synchronous rectifier improves the system efficiency, no control method for tracking $\eta_{\max}$ is required by Qi standard and used in Qi product. Then, it is reasonable to introduce $\eta_{\max}$ tracking for Qi product. With higher system efficiency, the wireless chargers would be more attractive to customers. Fig. 23 shows that $\eta_{\max}$ of Qi product is 75%. With the proposed control method, the system efficiency is higher than Qi product throughout the charging process and $\eta_{\max}$ is 77%. It is pointed out that the comparison in Fig. 23 is based on our laboratory test and parameters are made as similar as possible.

In the future works, system miniaturization and algorithm optimization will be performed to make the WPT system to be suitable for practical applications. The performance (such as the response speed and algorithm complexity) of the proposed P&O algorithm for $\eta_{\max}$ tracking can be further improved by using

TABLE V
SUMMARY AND COMPARISON OF THE PREVIOUS CONTROL METHODS

Reference	Operating Frequency (MHz)	Distance @ coupling coefficient	Maximum efficiency (%)	Secondary-side Circuit	Wireless communication link
[5] @2015	0.515	25 cm@0.04	74	Boost converter	Yes
[19] @2015	0.09765	10 cm@0.1	69	Buck-boost converter	No
[32] @2016	0.305	5.5 cm@0.137	76	Modified LSK circuit	Yes
[20] @2017	6.78	3 cm@0.09	51	Buck converter	Yes
[22] @2017	0.1	5 cm@0.168	85	Buck-boost converter	Yes
[33] @2017	0.917	50 cm@0.01	70	Half-bridge converter	No
[34] @2017	0.09765	20 cm@0.0689	73	On-off switch	Yes
This paper	0.0855	3 cm@0.15	81	Semi-active rectifier	No

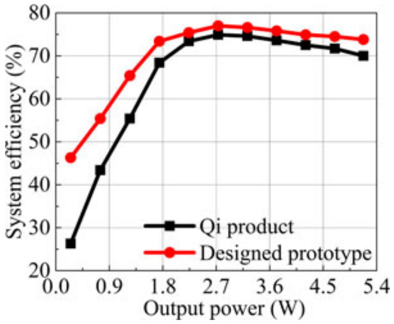

Fig. 23. System efficiency comparison between the designed WPT system and Qi product.

the optimization algorithms that are proven and widely used in the photovoltaic generation applications [35], [36].

VI. CONCLUSION

This paper proposes a WPT system that realizes CC charging and maximum efficiency tracking for SC. First, the influence of equivalent load resistance of the SC on charging current and efficiency is analyzed. By measuring the secondary-side resonant current, the phase between the input current and input voltage of the semiactive rectifier is synchronized. Then, the equivalent input impedance is purely resistive that ensures a high efficiency. Furthermore, the PI controlled secondary-side semiactive rectifier is used to achieve CC charging. Second, combined with the phase shift H-bridge inverter that is controlled by the P&O algorithm, the maximum efficiency tracking is realized by searching the minimum system dc input current for a given output power. Finally, theoretical analysis are validated by simulations and experiments. The results show that not only CC charging is achieved, but also the efficiency is significantly improved. The proposed control method is attractive for the applications that require compact receiver and no wireless communication link.

REFERENCES

[1] S. Lee, B. Chao, and C. T. Rim, “Dynamics characterization of the inductive power transfer system for online electric vehicles by Laplace phasor transform,” *IEEE Trans. Power Electron.*, vol. 28, no. 12, pp. 5902–5909, Dec. 2013.

[2] S. Li and C. Mi, “Wireless power transfer for electric vehicle applications,” *IEEE J. Emerging Sel. Top. Power Electron.*, vol. 3, no. 1, pp. 4–17, Mar. 2015.

[3] G. A. Covic and J. T. Boys, “Modern trends in inductive power transfer for transportation applications,” *IEEE J. Emerg. Sel. Top. Power Electron.*, vol. 1, no. 1, pp. 28–41, Jun. 2015.

[4] G. Buja, M. Bertoluzzo, and K. N. Mude, “Design and experimentation of WPT charger for electric city-car,” *IEEE Trans. Ind. Electron.*, vol. 62, no. 62, pp. 7436–7447, Dec. 2015.

[5] H. Li, J. Li, K. Wang, W. Chen, and Y. Xu, “A maximum efficiency point tracking control scheme for wireless power transfer systems using magnetic resonant coupling,” *IEEE Trans. Power Electron.*, vol. 30, no. 7, pp. 3998–4008, Jul. 2015.

[6] N. Liu and T. G. Habetler, “Design of a universal inductive charger for multiple electric vehicle models,” *IEEE Trans. Power Electron.*, vol. 30, no. 11, pp. 6378–6390, Nov. 2015.

[7] S. Kim, G. Covic, and J. Boys, “Tripolar pad for inductive power transfer systems for EV Charging,” *IEEE Trans. Power Electron.*, vol. 32, no. 7, pp. 5045–5057, Jul. 2017.

[8] X. Lu, D. Niyato, P. Wang, D. I. Kim, and Z. Han, “Wireless charger networking for mobile devices: Fundamentals, standards, and applications,” *IEEE Wireless Commun.*, vol. 22, no. 2, pp. 126–135, Apr. 2015.

[9] K. E. Koh, T. C. Beh, T. Imura, and Y. Hori, “Impedance matching and power division using impedance inverter for wireless power transfer via magnetic resonant coupling,” *IEEE Trans. Ind. Appl.*, vol. 50, no. 3, pp. 2061–2070, May/Jun. 2014.

[10] Z. Li, C. Zhu, J. Jiang, K. Song, and G. Wei, “A 3 kW wireless power transfer system for sightseeing car supercapacitor charge,” *IEEE Trans. Power Electron.*, vol. 32, no. 5, pp. 3301–3316, Jun. 2017.

[11] K. Colak, E. Asa, M. Bojarski, D. Czarkowski, and O. C. Onar, “A novel phase-shift control of semibridgeless active rectifier for wireless power transfer,” *IEEE Trans. Power Electron.*, vol. 30, no. 11, pp. 6288–6297, Nov. 2015.

[12] W. Zhang, S. C. Wong, C. K. Tse, and Q. Chen, “Design for efficiency optimization and voltage controllability of series–series compensated inductive power transfer systems,” *IEEE Trans. Power Electron.*, vol. 29, no. 1, pp. 191–200, Jan. 2014.

[13] Y. Lim, H. Tang, S. Lim, and J. Park, “An adaptive impedance-matching network based on a novel capacitor matrix for wireless power transfer,” *IEEE Trans. Power Electron.*, vol. 29, no. 8, pp. 4403–4413, Aug. 2014.

[14] T. C. Beh, M. Kato, T. Imura, S. Oh, and Y. Hori, “Automated impedance matching system for robust wireless power transfer via magnetic resonance coupling,” in *IEEE Trans. Ind. Electron.*, vol. 60, no. 9, pp. 3689–3698, Sep. 2013.

[15] G. Lee, B. H. Waters, Y. G. Shin, J. R. Smith, and W. S. Park, “A reconfigurable resonant coil for range adaptation wireless power transfer,” *IEEE Trans. Antennas Propag.*, vol. 64, no. 2, pp. 624–632, Feb. 2016.

[16] F. Mirzavand, V. Nayyeri, M. Soleimani, and R. Mirzavand, “Efficiency improvement of WPT system using inexpensive auto-adaptive impedance matching,” *Electron Lett.*, vol. 52, no. 25, pp. 2055–2057, Dec. 2016.

[17] A. P. Sample, D. A. Meyer, and J. R. Smith, “Analysis, experimental results, and range adaptation of magnetically coupled resonators for wireless power transfer,” *IEEE Trans. Ind. Electron.*, vol. 58, no. 2, pp. 544–554, Feb. 2011.

[18] H. Feng, T. Cai, S. Duan, J. Zhao, X. Zhang, and C. Chen, “An LCC compensated resonant converter optimized for robust reaction to large coupling variation in dynamic wireless power transfer,” *IEEE Trans. Ind. Electron.*, vol. 63, no. 10, pp. 6591–6601, Oct. 2016.

[19] W. X. Zhong and S. Y. R. Hui, “Maximum energy efficiency tracking for wireless power transfer systems,” *IEEE Trans. Power Electron.*, vol. 30, no. 7, pp. 4025–4034, Jul. 2015.

[20] T. Yeo, D. Kwon, S. Khang, and J. Yu, “Design of maximum efficiency tracking control scheme for closed-loop wireless power charging system employing series resonant tank,” *IEEE Trans. Power Electron.*, vol. 32, no. 1, pp. 471–478, Jan. 2017.

[21] Z. Huang, S. C. Wang, and C. K. Tse, “Control design for optimizing efficiency in inductive power transfer systems,” *IEEE Trans. Power Electron.*, to be published.

[22] X. Dai, X. Li, Y. Li, and P. Hu, “Maximum efficiency tracking for wireless power transfer systems with dynamic coupling coefficient estimation,” *IEEE Trans. Power Electron.*, to be published.

[23] M. Fan, C. Ma, and X. Zhu, “A cascaded boost–buck converter for high-efficiency wireless power transfer systems,” *IEEE Trans. Ind. Inform.*, vol. 10, no. 3, pp. 1971–1980, Nov. 2014.

[24] J. Sallán, J. L. Villa, A. Llombart, and J. F. Sanz, “Optimal design of ICPT systems applied to electric vehicle battery charge,” *IEEE Trans. Ind. Electron.*, vol. 56, no. 6, pp. 2140–2149, Jun. 2009.

[25] R. Mai, C. Y. Liu, Y. Li, P. Yue, and Z. He, “An active-rectifier-based maximum efficiency tracking method using an additional measurement coil for wireless power transfer,” *IEEE Trans. Power Electron.*, vol. 33, no. 1, pp. 716–728, Jan. 2018.

[26] J. H. Teng, W. H. Huang, T. A. Hsu, and C. Y. Wang, “Novel and fast maximum power point tracking for photovoltaic generation,” *IEEE Trans. Ind. Electron.*, vol. 63, no. 8, pp. 4955–4966, Aug. 2016.

[27] M. Fu, H. Yin, X. Zhu, and C. Ma, “Analysis and tracking of optimal load in wireless power transfer systems,” *IEEE Trans. Power Electron.*, vol. 30, no. 7, pp. 3952–3963, Jul. 2015.

[28] C. R. Sullivan, “Computationally efficient winding loss calculation with multiple windings, arbitrary waveforms, and two-dimensional or three dimensional field geometry,” *IEEE Trans. Power Electron.*, vol. 16, no. 1, pp. 142–150, Jan. 2001.

[29] E. Gati, G. Kampitsis, and S. Manias, “Variable frequency controller for inductive power transfer in dynamic conditions,” *IEEE Trans. Power Electron.*, vol. 32, no. 2, pp. 1684–1696, Feb. 2017.

[30] S. Y. Hui, “Planar wireless charging technology for portable electronic products and Qi,” *Proc. IEEE*, vol. 101, no. 6, pp. 1290–1301, Jun. 2013.

[31] 2018. [Online]. Available: http://www.wirelesspowerconsortium.com/

[32] D. Ahn, S. Kim, J. Moon, and I.-K. Cho, “Wireless power transfer with automatic feedback control of load resistance transformation,” *IEEE Trans. Power Electron.*, vol. 31, no. 11, pp. 7876–7886, Nov. 2016.

[33] H. Li, J. Fang, S. Chen, K. Wang, and Y. Tang, “Pulse density modulation for maximum efficiency point tracking of wireless power transfer systems,” *IEEE Trans. Power Electron.*, to be published.

[34] W. Zhong and S. Y. R. Hui, “Maximum energy efficiency operation of series-series resonant wireless power transfer systems using on-off keying modulation,” *IEEE Trans. Power Electron.*, vol. 33, no. 4, pp. 3595–3603, Apr. 2018.

[35] Y. Jiang, J. A. A. Qahouq, and T. A. Haskew, “Adaptive step size with adaptive-perturbation-frequency digital MPPT controller for a singlesensor photovoltaic solar system,” *IEEE Trans. Power Electron.*, vol. 28, no. 7, pp. 3195–3205, Jul. 2013.

[36] M. Boztepe, F. Guinjoan, G. Velasco-Quesada, S. Silvestre, A. Chouder, and E. Karatepe, “Global MPPT scheme for photovoltaic string inverters based on restricted voltage window search algorithm,” *IEEE Trans. Ind. Electron.*, vol. 61, no. 7, pp. 3302–3312, Jul. 2014.

Zhenjie Li (S’18) received the B.S. degree in measurement and control technology and instrument from the School of Measurement and Control Technology and Communication Engineering, Harbin University of Science and Technology, Harbin, China in 2012, and M.S. degree in instrument science and technology from the School of Electrical Engineering and Automation, Harbin Institute of Technology, Harbin, China in 2014, where he is currently working toward the Ph.D. degree in instrument science and technology.

His research interests include the design and analysis of wireless power transfer systems for supercapacitor and battery charge.

Kai Song (M’12) received the B.S., M.S., and Ph.D. degrees in instrument science and technology from the Harbin Institute of Technology (HIT), Harbin, China, in 2005, 2007 and 2011, respectively.

In 2011, he joined the School of Electrical Engineering and Automation, HIT, as a lecturer, and was a visiting scholar in electrical engineering, University of Tokyo, Tokyo, Japan, from 2014 to 2015. Since 2016, he has been working as an Associate Professor with the School of Electrical Engineering and Automation, HIT.

His current research interests concentrate in wireless power transfer, particularly in high-power wireless power transfer systems for electric vehicles and robots.

Jinhai Jiang received the B.S. degree in measurement and control technology and instrument from the School of Electronic Science, Northeast Petroleum University, Daqing, China in 2010, and the M.S. degree in electrical engineering from the School of Electrical Engineering and Information from Northeast Petroleum University, Daqing, China in 2013. He is currently working toward Ph.D. degree in electrical engineering at Harbin Institute of Technology.

His research interests include wireless power transfer for supercapacitors and battery powered online electric vehicles.

Chunbo Zhu (M’05) received the B.S. and M.S. degrees in electrical engineering and the Ph.D. degree in mechanical engineering from the Harbin Institute of Technology (HIT), Harbin, China, in 1987, 1992, and 2001, respectively.

He was a Post-Doctoral Research Fellow with the PEI Research Center, National University of Ireland, Galway, Ireland, from 2003 to 2004. Since 1987, he has been a Lecturer with the Department of Automation Measurement and Control, HIT. He is currently a Full Professor with HIT, where he leads the Laboratory of Wireless Power Transfer and Battery Management Technologies. His current research interests include energy management systems, electric and hybrid electric vehicles, and wireless power transfer technologies.